



Formulation and assessment of flamelet-generated manifolds for reacting interfaces

Brian T. Bojko, Paul E. DesJardin*

Department of Mechanical and Aerospace Engineering, University at Buffalo, the State University of New York, Buffalo, NY 14260-4400, United States



ARTICLE INFO

Article history:

Received 1 June 2016

Revised 29 June 2016

Accepted 9 August 2016

Available online 13 September 2016

Keywords:

Flamelet-generated manifold

Biomass

Modeling

ABSTRACT

The coupling of heat and mass transfer at the surface of solid or liquid fuels is important when modeling near-surface gasification and combustion processes. Modeling the reacting boundary layer with the use of finite-rate chemistry allows for a highly accurate description of the coupling between the flame and fuel surface, but is not tractable when considering detailed chemical kinetic mechanisms. In this study, simplified unsteady 1D flames with mass blowing are considered for a solid biomass fuel where the flamelet-generated manifold (FGM) method is employed as a model reduction strategy for potential application to multidimensional calculations, such as flame spread over solid materials undergoing pyrolysis and ablation. Two types of FGM are considered. The first are a set of steady-state flames differentiated by their scalar dissipation rate. Steady flamelets have been used extensively in the past for jets, shear-layers, etc. but, their application to solid fuel boundaries is new. Results show that the use of steady flames produce unacceptable errors, with temperature errors in excess of 45%. To avoid these errors, a new methodology for developing an unsteady FGM is presented that accounts for unsteady diffusion effects but, is also independent of surface mass flux. Results using the unsteady FGM greatly reduces errors in temperature with differences that are under 10%.

© 2016 The Combustion Institute. Published by Elsevier Inc. All rights reserved.

1. Introduction

The flamelet-generated manifold (FGM) [1–3] method has been used to describe premixed flames [4,5] and non-premixed flames [3,6] with extensions to multi-dimensional turbulent combustion environments. Recently, Knudsen and Pitsch [7] have studied the combination of premixed and non-premixed flamelets to assess their mutual application to describe partially-premixed combustion environments. Wu et al. [8] introduced the Pareto-efficient combustion model for predicting and modeling multi-regime flames. Vreman et al. [9] and Ihme et al. [10] have successfully applied the FGM method to complex turbulent combustion simulations of the experimental set of Sandia D and E flames developed by Barlow et al. [11]. The FGM approach has also been extended to modeling dilute spray combustion including *n*-heptane [12], α -methylnaphthalene/*n*-decane [13], *n*-dodecane [14], acetone sprays [15], and Jet-A fuel [16].

Reacting boundary layers of solid/liquid fuels requires an accurate description of the surface heat flux in order to sufficiently model the coupling of heat and mass transfer at the surface under-

going gasification as well as, for determining the resulting flame configuration. The mass flux at the solid/liquid surface can result in unsteady diffusion flames in multidimensional burning configurations such as upward flame-spread and burning propellant in solid rockets. For this class of flames, Xie and DesJardin developed an embedded flame modeling approach where the governing equations for the conjugate heat and mass transfer between a solid and fluid interface are described [17]. The coupling method was applied to DNS of upward flame spread of solid poly(methyl methacrylate) (PMMA) undergoing pyrolysis [18]. Model reduction of the DNS results were conducted to reduce the degrees of freedom of the problem, but rely on collapsing the entire DNS solution to generate the reduced lookup table. The FGM has an advantage in that it maintains generality by storing the finite-rate chemistry source terms of individual flames instead of needing multiple, particular flame spread solutions to generate the manifold. The goal of this study is to extend the work of Xie and DesJardin by investigating the application of flamelet-generated manifolds for solid biomass combustion with constant mass blowing through the assessment of a steady and unsteady FGM approach.

The rest of this study is organized as follows. In Section 2.1, the governing equations and boundary conditions for the 1D reacting boundary layer are presented. Section 2.2, describes how the boundary conditions are determined through the use of a

* Corresponding author.

E-mail addresses: btbojko@gmail.com (B.T. Bojko), ped3@buffalo.edu (P.E. DesJardin).

multiphase equilibrium solver to evaluate pyrolysis species composition of the solid fuel. In Sections 3.1 and 3.2, two FGM modeling methodologies are presented. The first is a steady FGM approach constructed from the steady-state 1D diffusion flame solutions. The second approach uses unsteady diffusion flame solutions to create the unsteady FGM method. Results of the exact solution to the 1D reacting boundary layer are presented in Section 4.1. Validation of the steady FGM approach without mass blowing is conducted in Section 4.2, and then comparisons of the steady and unsteady FGM are made to the exact solution of 1D flames with mass blowing. Finally, conclusions are drawn on the application of steady and unsteady FGM.

2. Problem description

2.1. Reacting boundary in 1D

The gas phase solution is considered one-dimensional, fully compressible and viscous, resulting in the following set of conservation equations for mass, species, momentum and energy,

$$\frac{\partial \rho}{\partial t} + \frac{\partial(\rho u_x)}{\partial x} = 0 \quad (1a)$$

$$\frac{\partial(\rho Y_i)}{\partial t} + \frac{\partial(\rho u_x Y_i)}{\partial x} = \frac{\partial}{\partial x} \left(\rho D_i \frac{\partial Y_i}{\partial x} \right) + \dot{w}_i \quad (1b)$$

$$\frac{\partial(\rho u_x)}{\partial t} + \frac{\partial(\rho u_x^2)}{\partial x} = -\frac{\partial p}{\partial x} + \frac{\partial}{\partial x} \left(\mu \frac{\partial u_x}{\partial x} \right) \quad (1c)$$

$$\begin{aligned} \frac{\partial(\rho e_t)}{\partial t} + \frac{\partial}{\partial x} (\rho u_x H_t) &= \frac{\partial}{\partial x} \left(u_x \mu \frac{\partial u_x}{\partial x} \right) \\ &+ \frac{\partial}{\partial x} \left(k \frac{\partial T}{\partial x} + \sum_i^N \rho D_i \frac{\partial Y_i}{\partial x} h_i \right) - \sum \dot{w}_i h_{f,i}^o \end{aligned} \quad (1d)$$

where, \dot{w}_i is the mass consumption or production rate of the i th species, $e_t (= e + u_x^2/2)$ is the total sensible energy, $H_t (= e_t + p/\rho)$ is the total enthalpy, and $h_{f,i}^o$ is the heat of formation of the i th species. Assuming constant diffusivity, it can be shown [19] that, $\left(k \frac{\partial T}{\partial x} + \sum_i^N \rho D_i \frac{\partial Y_i}{\partial x} h_i \right)$, can be expressed as,

$$\mu \frac{c_p}{Pr} \left(1 - \frac{1}{Le} \right) \frac{dT}{dx} + \frac{1}{Sc} \frac{dh}{dx} \quad (2)$$

where, Pr is the Prandtl number, Sc is the Schmidt number, Le is the Lewis number, and h is the sensible enthalpy. Although differential diffusion is important, it has been neglected here to maintain a one-to-one correlation between the exact solution and transport equations for Z and C when comparing to the FGM implementation and to simplify the interpretation of results. Prandtl (Pr) and Schmidt (Sc) numbers are both set equal to 0.707, resulting in a unity Lewis number assumption. Viscosities are determined from the Sutherland viscosity model, while thermal and molecular diffusivities are calculated using the definitions of Pr and Sc respectively. Molecular fluxes are approximated using a second-order centered differencing approach, employing a semi-implicit operator to avoid diffusion time step stability limitations. The boundary conditions for the mass, species, and energy are explicitly set at the surface by imposing a total convective mass flux and specifying the species mass fractions and temperature at the solid/gas interface. Species and temperature at the surface are determined from a multiphase chemical equilibrium solution and mass fluxes are set to values typical of biomass combustion, to be discussed.

A finite volume method is used to solve the coupled system of non-linear equations and a second-order fractional step

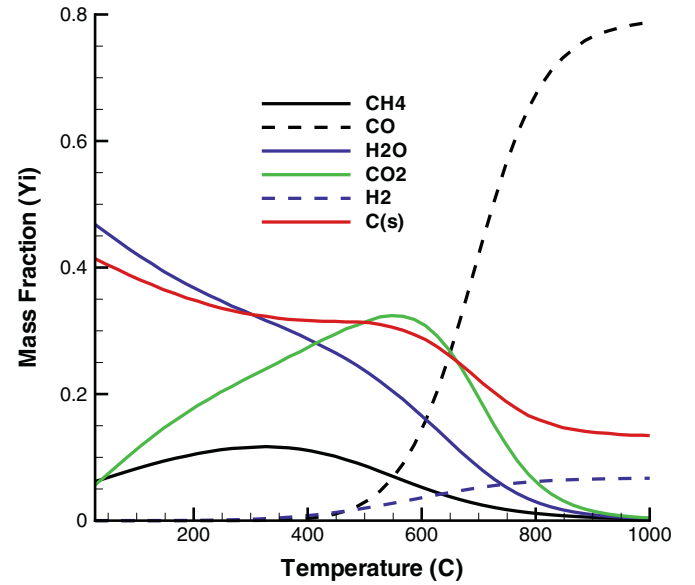
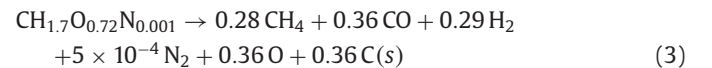


Fig. 1. Equilibrium composition of major species for wood undergoing pyrolysis at various temperatures.

method is used to integrate the equations using a two-stage Runge–Kutta time integration. Convective fluxes are discretized using an AUSM+UP flux vector splitting [20] with a combination of second-order upwind biased and essentially non-oscillatory (ENO) interpolants for determining fluxes [21,22]. The GRI-Mech 3.0 [23], consisting of 53 species and 325 reactions, is used to describe the combustion of pyrolysis gases, which is an appropriate choice considering the primary combustibles are CH_4 and CO . While the kinetic mechanism is not specifically tailored for biomass decomposition into tar and char, the objective of this study is to assess the FGM method applied to biomass-like combustion and is expected to be insensitive to these assumptions.

2.2. Fuel boundary

To determine the values of $Y_{i,s}$ at the fuel boundary a local multiphase chemical equilibrium is assumed. For this study, the interest lies in the solid biomass combustion of wood, where the fuel is assumed to be composed of, $\text{CH}_{1.7}\text{O}_{0.72}\text{N}_{0.001}$. A one-step atomic balance is used to estimate the chemical decomposition of the solid fuel into a set of realizable species expressed as,



where, thermodynamic properties are readily available for the species on the R.H.S. of Eq. (3). This composition is used as an input into a multiphase equilibrium solver using a Gibbs minimization procedure and elemental conservation which is solved using an algorithm similar to that in STANJAN [24].

Figure 1 shows pyrolysis products as a function of temperature. The char yield is estimated by $C(s)$, when this value plateaus at 31.5% for temperatures between 300°C and 550°C is when the main pyrolysis event occurs, consistent with values reported in the literature from thermal degradation experiments conducted with a batch reactor [25]. As the temperature increases further beyond 550°C, the CO_2 begins to decompose and the major species within the pyrolysis gases transitions to carbon-monoxide. Using the center of the region where the 31.5% char yield is constant to define the active gasification region, the pyrolysis temperature, $T_s = T_{\text{pyr}}$, is chosen to be 425°C (700K) and is typical of reported pyrolysis temperatures [26,27]. At this temperature the major

Table 1
Dirichlet boundary conditions for the pyrolysis species mass fractions and temperature at the fuel surface.

Pyrolysis property	Value
CH ₄	0.151
CO	0.010
H ₂ O	0.398
CO ₂	0.426
N ₂	7.03E – 4
H ₂	0.015
T	700 K

combustible species are methane and carbon monoxide. Carbon monoxide consists of roughly 1% of the total composition by mass, methane consists of only about 10% and the most abundant pyrolysis species are CO₂ and H₂O at ~27% each. These findings are consistent with the results of Bajus [25] and Wei et al. [28] for pyrolysis products from wood.

3. FGM formulation

3.1. Steady flames

In 1D Cartesian coordinates, the only valid steady solution of Eq. (1) is the limit when the total mass flux is zero. In this limit, the velocity field is zero ($u_x = 0$) and Eq. (1) reduces to,

$$\frac{\partial}{\partial x} \left(\rho D \frac{\partial Y_i}{\partial x} \right) + \dot{w}_i = 0 \quad (4a)$$

$$\frac{\partial}{\partial x} \left(\mu \frac{c_p}{Pr} \left(1 - \frac{1}{Le} \right) \frac{\partial T}{\partial x} + \frac{1}{Sc} \frac{\partial h}{\partial x} \right) - \sum \dot{w}_i h_{f,i}^o = 0 \quad (4b)$$

where, pressure work and viscous dissipation are neglected. The system of non-linear equations are solved on discrete domain lengths (L) using a time marching technique until steady-state is reached. Dirichlet boundary conditions are used for the fuel and air side, where the fuel boundary conditions for species and temperature are set equal to the pyrolysis gas phase species mass fractions and the pyrolysis temperature, values shown in Table 1. Since a steady-state solution is only possible with the constraint $\dot{m}_f'' = 0$, the sum of individual species mass fluxes must equal zero at every location. Also, considering \dot{m}_f'' is non-zero at the fuel boundary, this assumption implies that products of combustion diffuse back and are absorbed into the solid. The air-side boundary is a Dirichlet boundary at standard conditions, $Y_{O_2} = 0.23$, $Y_{N_2} = 0.77$, $T_{air} = 300$ K, and $P_{air} = 1$ atm. In this study all air side boundary conditions are set to standard conditions, while the type of boundary, i.e. Dirichlet or Natural, is explicitly stated. Once steady-state is obtained, L is reduced and the solution procedure continues until L is so small that a diffusion flame cannot be maintained. The steady solutions are cataloged by the physical size of the flame domain, L , for which their corresponding scalar dissipation rate, $\chi = 2D(L^2)^{-1}$, is constant. Figure 2(a) shows the temperature profiles of several steady flames for decreasing values of L . As χ increases, diffusion of heat away from the flame increases until extinguishment occurs. Extinguishment occurs at $L = 2.1$ mm corresponding to quenching scalar dissipation rate of $\chi_q \approx 115$ s⁻¹, which is approximately twice as large as χ_q for pure methane flames and is a direct result of the pyrolysis boundary conditions containing products species.

Figure 2(b) shows the flames of Fig. 2(a) in terms of the mixture fraction, Z . Λ in this figure is the value of the progress-variable, C , at the stoichiometric flame limit (Z_{st}) and varies between 0 and 1, corresponding to the pure mixing case and the equilibrium limit

Table 2
Species and associated weights used to define the progress-variable as determined from the cost function minimization procedure.

Species	Weight (α_i)
NH ₃	0.0
HCN	0.0
C ₂ H ₂	7.8E – 3
NO	1.0
HOCN	0.0
HCCOH	0.98
HNCO	0.0
NCO	0.0
C ₃ H ₇	9.1E – 4

respectively. The peak flame temperature is approximately 1900 K and is 1650 K just prior to extinguishment.

To account for the effects of χ on flame shape, the progress-variable defined as, $C = \sum_{i=1}^N \alpha_i(Y_i) / \sum_{i=1}^N \alpha_i(Y_{eq,i})_{st}$, is introduced, where the weighting factors, α_i , must be determined. Previous studies have often used linear combinations of CO₂, H₂O, H₂, and CO [9,29,30]. These combinations work well for simple boundaries where the products do not appear in either the fuel or air streams; however, for wood pyrolysis, off-gas fuel components are also combustion products. To compute α_i , a new method is developed based on the optimization strategy of Ihme et al. [30], where a cost function is minimized. The cost function is defined as,

$$\iint \left[\Omega H \left(\epsilon - \frac{\partial C}{\partial \Lambda} \right) + \Omega H(-C) \right] dZ d\Lambda \quad (5)$$

where, Ω is a penalty factor, H is the Heaviside function, ϵ is a small positive value and Λ is C_{st} . The first Heaviside function enforces monotonicity of C and is described in the method of Ihme et al.. The second Heaviside function introduced in this study encourages the weighted values to span as much of the $\Lambda - Z$ space possible, discouraging negative values of C and reducing manifold gradients of tabulated species and source terms. In this study, Ω is chosen to be the absolute value of the energy source term. Penalizing the cost function by the energy source term guarantees the most dynamic areas of the flame are accurately captured in the FGM. The numerical solution procedure to minimize the cost function is a multidimensional downhill simplex method [31].

Considering only species that are not in the pyrolysis gas and vary monotonically in Λ , results in the following species and weights, as shown in Table 2. Therefore, for the wood fuel considered in this study, NO, C₂H₂ and HCCOH are the most heavily weighted species. Figure 3(a) and (b) shows the contour of C and heat flux in $\Lambda - Z$ space respectively, where monotonicity and smoothness of C is observed. Figure 4(a) and (b) shows the trajectories of NO and C₂H₂, respectively, as a function of C for discrete values of mixture fraction that were chosen to bound $Z_{st} = 0.25$. Figure 4 verifies that the monotonicity constraint is satisfied and the species gradients are relatively low for the steady-state case. Once the α_i 's are defined then a mapping between any flame parameter, ϕ , originally expressed in $\Lambda - Z$ space, can be mapped to $Z - C$ space, i.e. $\phi = \phi(Z, C(\chi))$.

3.2. Unsteady flames

The question of whether or not a collection of steady-state solutions can be used to model unsteady flame effects has been studied extensively and modeling extensions have typically relied on either higher dimensional FGMs [32–34] or solving unsteady

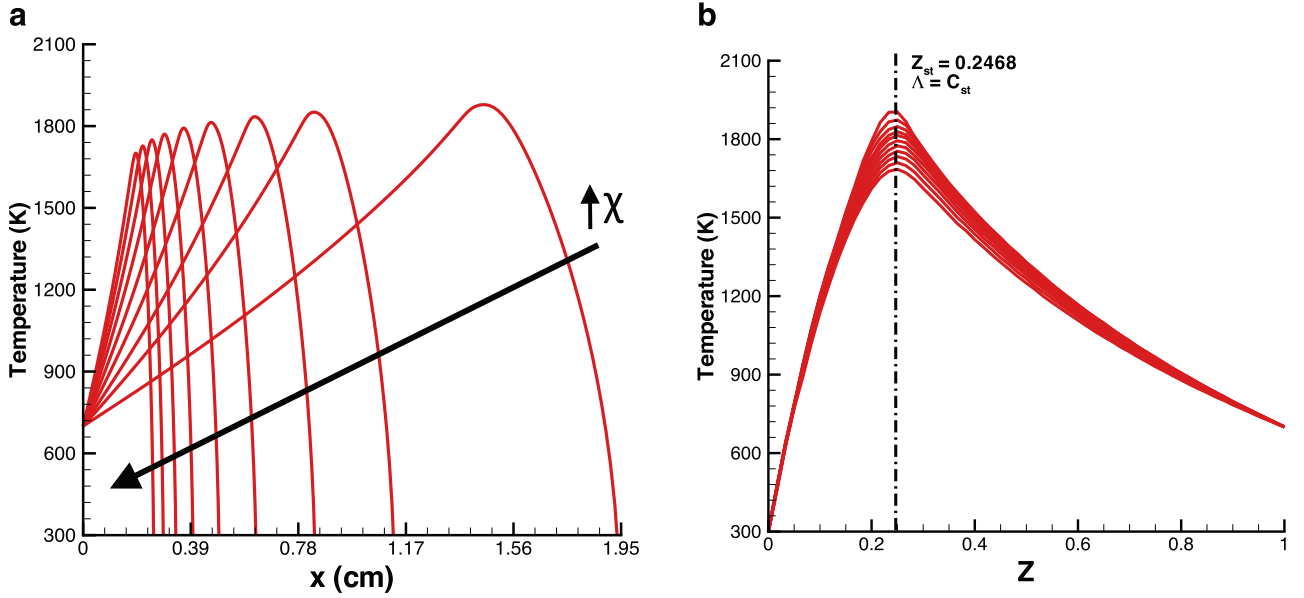


Fig. 2. Steady-state diffusion flames at (a) different domain lengths and (b) collapsed into Z -space showing the definition of Λ at the stoichiometric limit Z_{st} .

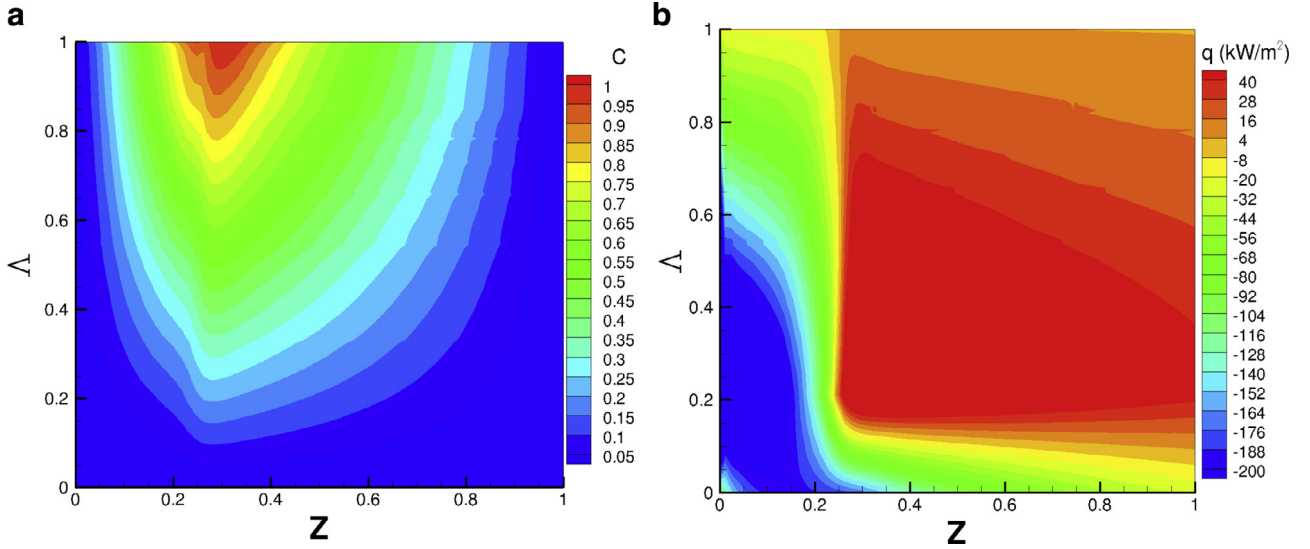


Fig. 3. Contour of the steady (a) progress-variable (C) and (b) the heat flux (kW/m^2) as a function of Λ and Z .

flamelet equations during runtime [35–37]. An accurate model of unsteady effects such as ignition/extinction, heat loss, pollutant formation (i.e. soot and NO_x), etc., is particularly important in regions where diffusion and kinetic time scales are comparable. Unsteady diffusion flamelets without convection have been studied by Pitsch et al. [35], where a time dependent analytical expression for χ is given considering a semi-infinite medium to account for its unsteady evolution during a flamelet solution. Ihme et al. [38] explored unsteady flamelet effects to predict autoignition by solving the unsteady flamelet equations at specified values of χ , such that the flame properties were a function of Z , C , and χ . Instead of relying on the unsteady analytical solution or specified functional form of χ , or a multidimensional manifold, the objective of this study is to capture the effects of the unsteady progression of $\chi = \chi(t)$ during the expansion of a diffusion flame in physical coordinates and catalog the results using the progress-variable definition.

Investigating the analytical solution to the 1D unsteady transport equation for mixture fraction with mass blowing is used to determine the necessary requirements for developing the unsteady FGM. Assuming constant density, species diffusivity and mass flux

the transport equation of the mixture fraction can be expressed as,

$$\rho \frac{\partial Z}{\partial t} + \dot{m}_T'' \frac{\partial Z}{\partial x} = \rho D \frac{\partial^2 Z}{\partial x^2} \quad (6)$$

where the convection term can be eliminated through the transformation to $\eta - \tau$ space via relations analogous to the wave equation, $\eta = x - (\dot{m}_T''/\rho)t$ and $\tau = t$. In doing so, one obtains the transient diffusion equation, $\partial Z/\partial \tau = D(\partial^2 Z/\partial \eta^2)$, with constant diffusivity. Comparable to the solution procedure used to solve the transient 1D heat conduction equation on a finite domain [39], the Fourier series method is applied here to obtain an analytical expression for Z . The analytical expression for, $Z = Z(\eta, \tau)$, on a finite domain of width, L_η , is given as,

$$Z(\eta, \tau) = Z_1 - \frac{\eta(Z_1 - Z_2)}{L_\eta} - \frac{2}{L_\eta} \sum_{n=1}^{\infty} e^{-D\lambda_n^2 \tau} \sin \lambda_n \eta \times \left[\frac{Z_1 - (-1)^n Z_2}{\lambda_n} - \int_0^{L_\eta} f(\eta') \sin \lambda_n \eta' d\eta' \right] \quad (7)$$

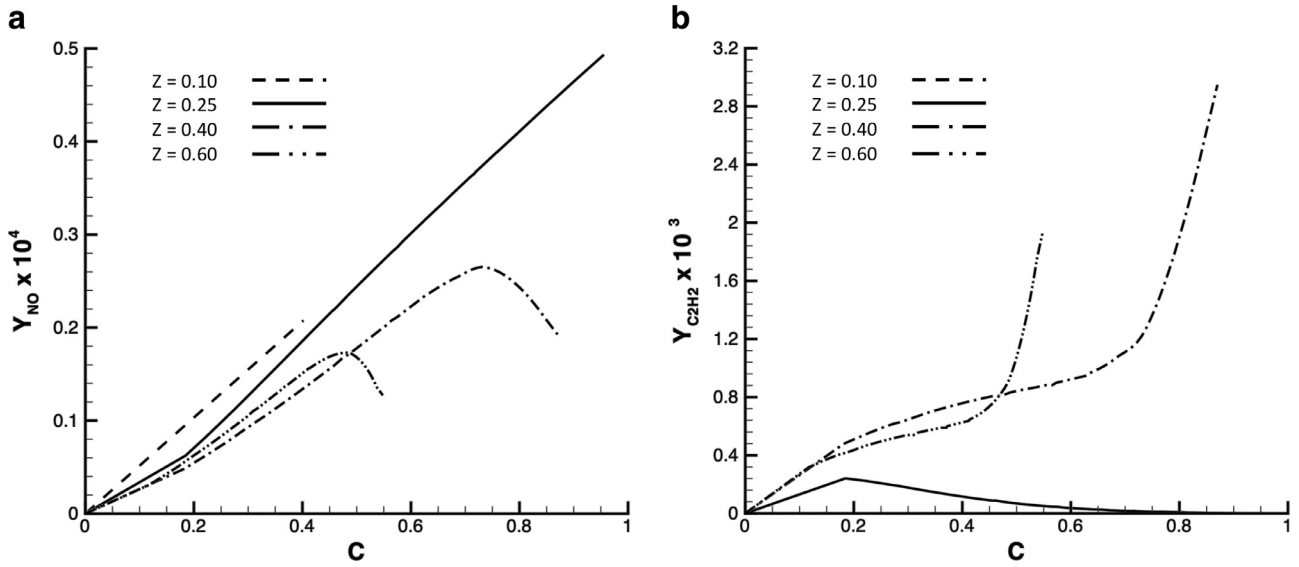


Fig. 4. Trajectories of (a) NO and (b) C_2H_2 as a function of C for discrete values of Z for the steady FGM.

where, \dot{m}_T''/ρ is assumed constant, $\lambda_n = n\pi/L_\eta$, $f(\eta')$ is the initial condition for $Z(x, 0) = Z(\eta, 0) = f$, and the Dirichlet boundary conditions are, $Z(0, \tau) = 1$ and $Z(L_\eta, \tau) = 0$. Mass blowing is absorbed into the definition of η . The corresponding analytical expression for $\chi = 2D|(dZ/d\eta)(d\eta/dx)|^2$ is then,

$$\chi(\eta, \tau) = 2D \left[Z_1 - \frac{(Z_1 - Z_2)}{L_\eta} - \frac{2}{L_\eta} \sum_{n=1}^{\infty} -\lambda_n e^{-D\lambda_n^2 \tau} \cos \lambda_n \eta \right. \\ \left. \times \left[\frac{Z_1 - (-1)^n Z_2}{\lambda_n} \right] \right]^2 \quad (8)$$

where, $d\eta/dx = 1$, and $f(\eta')$ from Eq. (7) is assumed 0 for simplicity. It is clear the leading order effect on χ is the exponential decay term, $\exp(-D\lambda_n^2 \tau)$, which is unaffected by \dot{m}_T'' . Therefore, the unsteady flames are defined by $\chi(t)$, and show a weak dependence on \dot{m}_T'' for relatively low blowing rates, where any value of \dot{m}_T'' can be used to generate the manifold using the unsteady computation.

Consequently, one can consider constructing a flamelet-generated manifold from a set of expanding diffusion flames with $\dot{m}_T'' = 0$ to capture the effects of the unsteady flame. The conservation equations in Eq. (4) are solved in their unsteady form by simply replacing the zeros on the R.H.S. of the equations with $\partial(\rho Y_i)/\partial t$ and $\partial(\rho e_t)/\partial t$ for species and energy, respectively. The same Dirichlet boundary conditions for air and fuel as defined in Table 1 and used in the steady solution are applied here for the unsteady diffusion flame solution. Figure 5(a) shows a series of flames starting from an initial flame configuration at $t = 0$ s with a large scalar dissipation rate of $\chi = 115 s^{-1}$ and associated length of ~ 2.1 mm. The initial flame is then allowed to diffuse outward to the far-field boundary with the maximum length of 4 cm. During this unsteady process the maximum value of product species and temperature exceed those found on the steady-state manifold, indicating the importance of the unsteady flame dynamics. The temperature increases from 1650 K, corresponding to the extinction limit, to over 2000 K and then decreases as the flame approaches a quasi steady-state solution. Figure 5(a) represents only 7 of the nearly 200 flames used to construct the manifold.

Figure 5(b) shows the temperature profiles as a function of Z with the line indicating where Λ exists for the unsteady flame solutions. One could consider using the optimization procedure as described above; however, the same values of α_i determined for the steady-state manifold are used for the sake of direct compar-

ison. The contour of C is shown in $\Lambda - Z$ space in Fig. 6(a), where monotonicity and smoothness are again achieved. The differences in the C -contours between the steady and unsteady FGMs show a narrower band of the progress-variable in the unsteady formulation. This corresponds to the increased values of species contributing to C as the flame progresses from a region where χ is large to a region of $\chi \approx 0$, opposed to a broader distribution of C observed in the steady FGM counterpart. Figure 6(b) shows the heat flux for the unsteady flames as a function of Λ and Z , with similar magnitudes as the steady FGM heat flux. The major differences in the heat flux appear between the flame and ambient air, where the values near the air are closer to zero for the unsteady conditions.

Figure 7(a) and (b) shows the trajectories of NO and C_2H_2 versus C at discrete values of Z , similar to the trajectories shown for the steady FGM. Although the weights determined from the steady-state solution and cost function analysis are used to create the unsteady FGM, the paths of NO and C_2H_2 show that monotonicity is again maintained. However, the gradients of the species are much steeper compared to their steady counterpart. Considering monotonicity is maintained between both the steady and unsteady FGM, the weights are kept constant between the two such that the only difference is the solution procedure of the flames used to create their respective manifold. In the unsteady case, all flame parameters, ϕ , can be mapped to Z and C similar to the steady case, except that χ is no longer set as a function of the solution domain and is rather allowed to freely form as the diffusion flame expands from high to low χ . Therefore, $\chi = \chi(t)$, and has a single trajectory in time and $\phi = \phi(Z, C(\chi(t)))$. The application of the unsteady FGM is not exclusive to boundaries with a convective flux, however, further investigation is required to assess its application to other practical scenarios where unsteady effects are important. By capturing the unsteady evolution of χ for different events, it is possible to catalog unsteady flame parameters as a function of Z and $C(\chi(t))$.

4. Results and discussion

4.1. Exact solution of unsteady flames with mass blowing

To assess the utility of the FGM for near-wall pyrolysis modeling (with reactions) with possible extensions to flame spread simulations, unsteady one-dimensional simulations are conducted at finite blowing rates. To investigate the reacting boundary layer

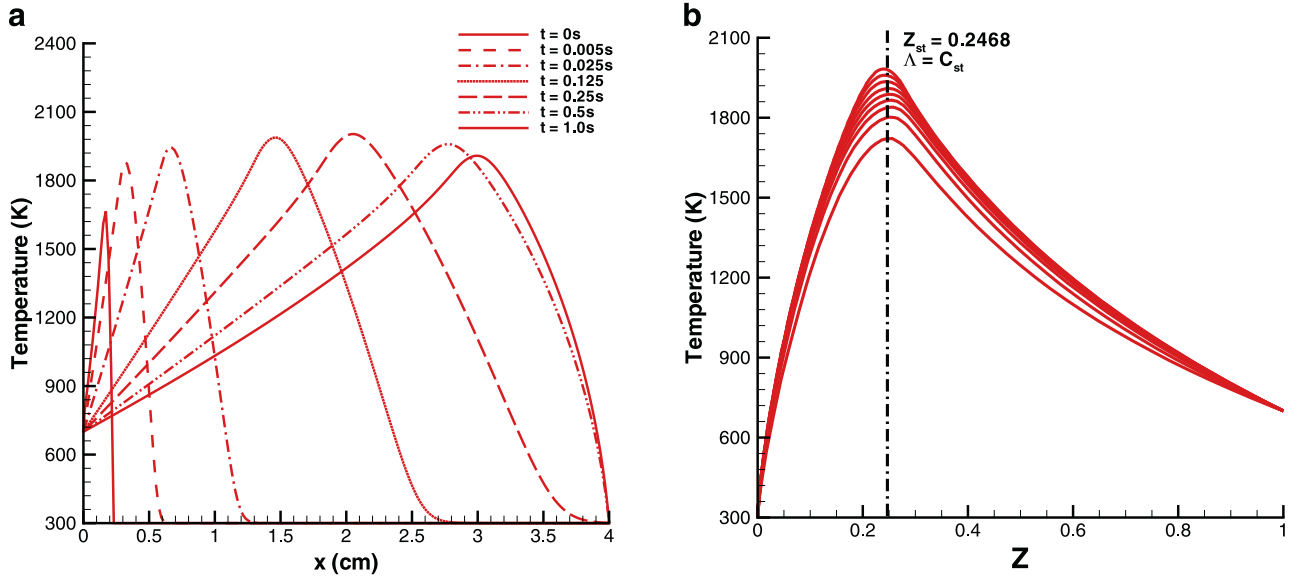


Fig. 5. Representation of the (a) unsteady flame progression of a diffusion flame from high to low values of χ and (b) the flames collapsed into Z -space indicating the location of Λ .

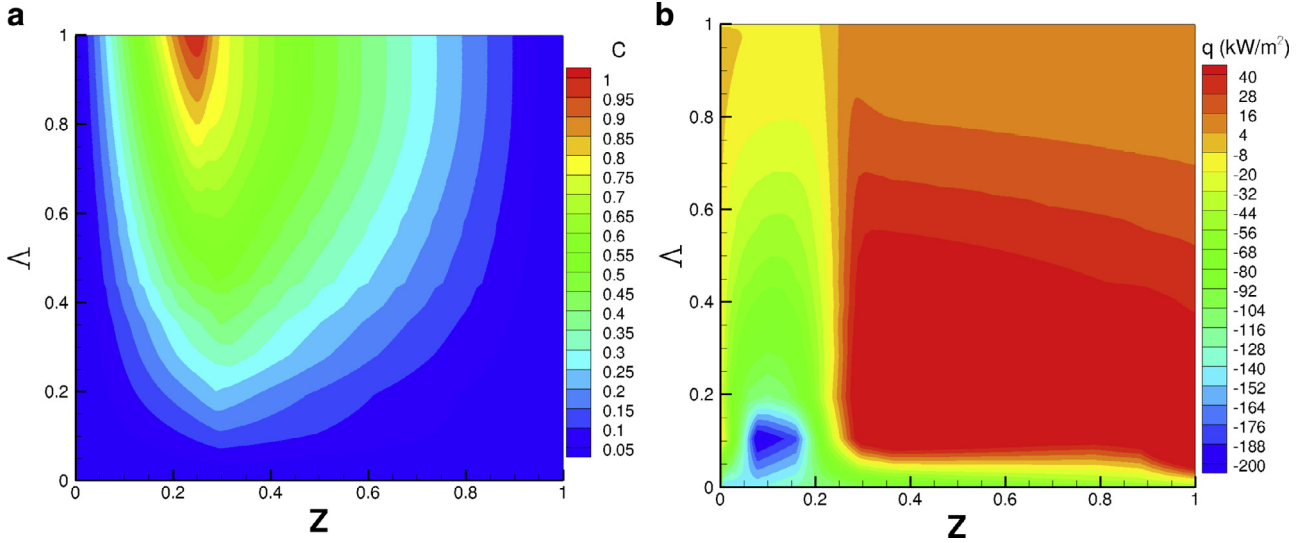


Fig. 6. Contour of the unsteady (a) progress-variable (C) and (b) the heat flux (kW/m^2) as a function of Λ and Z .

and application of the FGM approach, two different mass fluxes are used, with values of 0.01 and $0.02 \text{ kg/m}^2 \cdot \text{s}$, consistent with estimates of mass flux by Drysdale [40] for wood. The domain size explored has an overall length of $L = 3 \text{ cm}$ with 200 nodes resulting in a grid resolution of 0.15 mm to ensure a grid independent solution.

The boundary conditions for temperature, $T_{\text{pyr}} = 700 \text{ K}$, and gas phase species composition, $Y_{\text{CH}_4,s} = 0.151$, $Y_{\text{CO},s} = 0.01$, $Y_{\text{H}_2\text{O},s} = 0.398$, $Y_{\text{CO}_2,s} = 0.426$, $Y_{\text{H}_2,s} = 0.015$ are set at the fuel surface. The far-field conditions are set to ambient air with a natural boundary condition imposed such that the flame motion is unconstrained by the solution domain. The initial condition for the domain is a flame configuration in the first $1/6$ (5 mm) of the entire domain width, while the remainder of the region is set to ambient conditions. The starting flame configuration has an initial scalar dissipation rate of, $\chi_{st} = 41 \text{ s}^{-1}$, which is approximately $1/3$ of the initial value used to generated the unsteady FGM. The solution of Eq. (1) with the imposed Dirichlet boundary conditions, is presented in Fig. 8(a) for the temperature and major species, and

Fig. 8(b) for the heat flux at times of 0.1 and 0.2 s . Starting from the initial flame width, the flame is pushed out to the right and broadened as it is transversed out of the domain. It is interesting to note that combustion products CO_2 and H_2O never increase in magnitude beyond their values at the solid fuel boundary undergoing pyrolysis. This is an important feature of solid fuel combustion which increases the difficulty of defining the progress-variable.

4.2. FGM comparisons

Consistent with the exact solutions, an equal diffusivity assumption is used in Eq. (1) for direct comparison to the manifold method. The following transport equations for Z and C are solved,

$$\frac{\partial(\rho Z)}{\partial t} + \frac{\partial(\rho u_x Z)}{\partial x} = \frac{\partial}{\partial x} \left(\rho D \frac{\partial Z}{\partial x} \right) \quad (9a)$$

$$\frac{\partial(\rho C)}{\partial t} + \frac{\partial(\rho u_x C)}{\partial x} = \frac{\partial}{\partial x} \left(\rho D \frac{\partial C}{\partial x} \right) + \dot{S}_C''' \quad (9b)$$

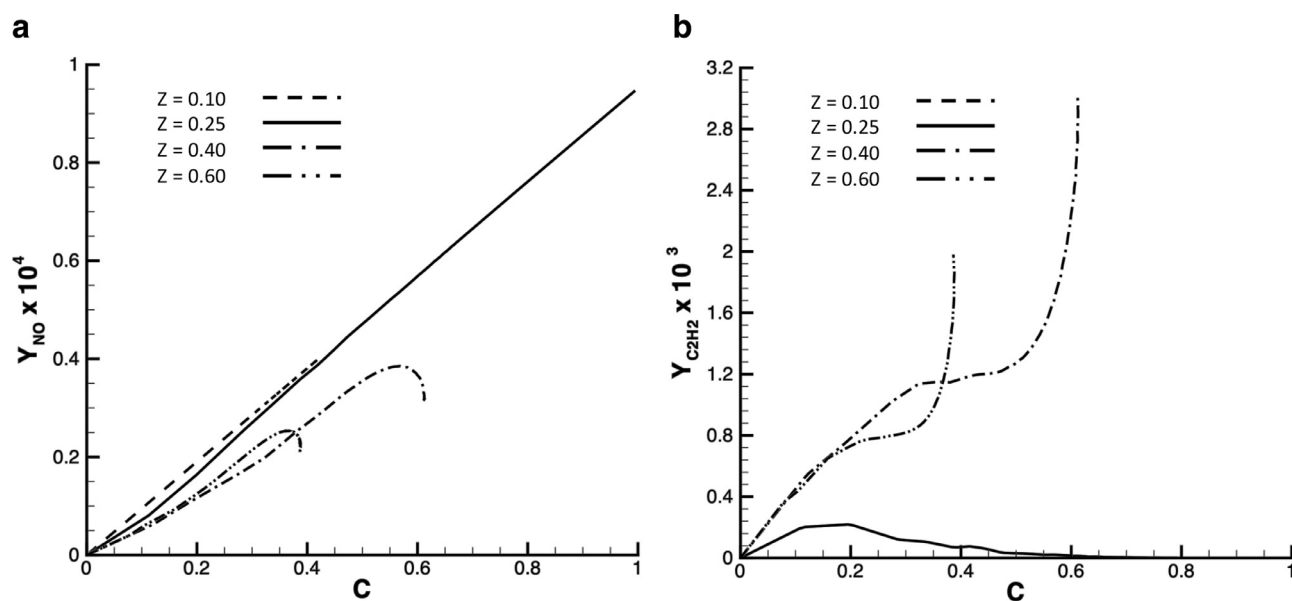


Fig. 7. Trajectories of (a) NO and (b) C_2H_2 as a function of C for discrete values of Z for the unsteady FGM.

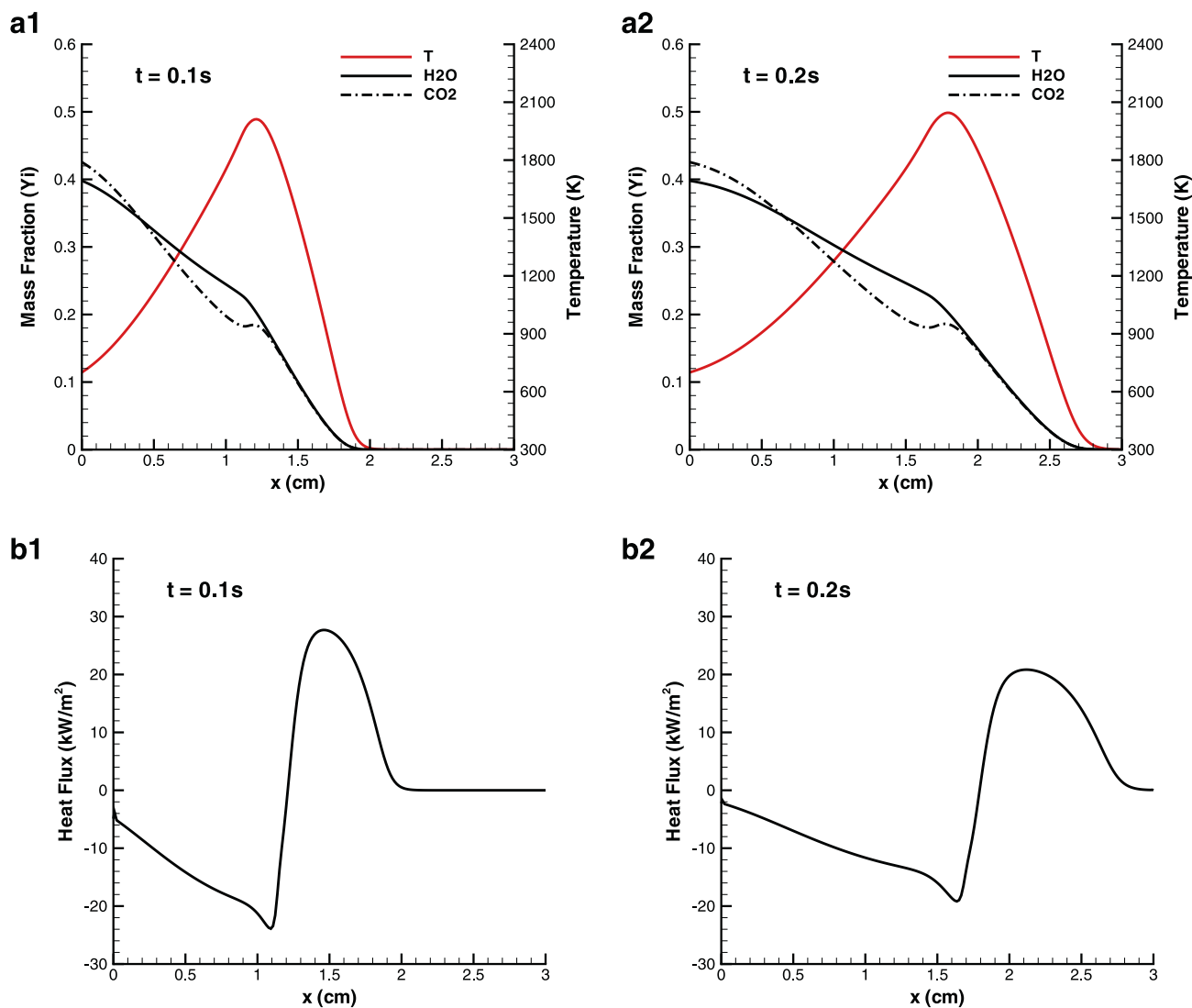


Fig. 8. One-D reacting boundary layer solutions for (a) temperature and major species and (b) heat flux with an applied mass flux of $0.02 \text{ (kg/m}^2 \cdot \text{s)}$ at the solid surface and for a domain width of 3 cm.

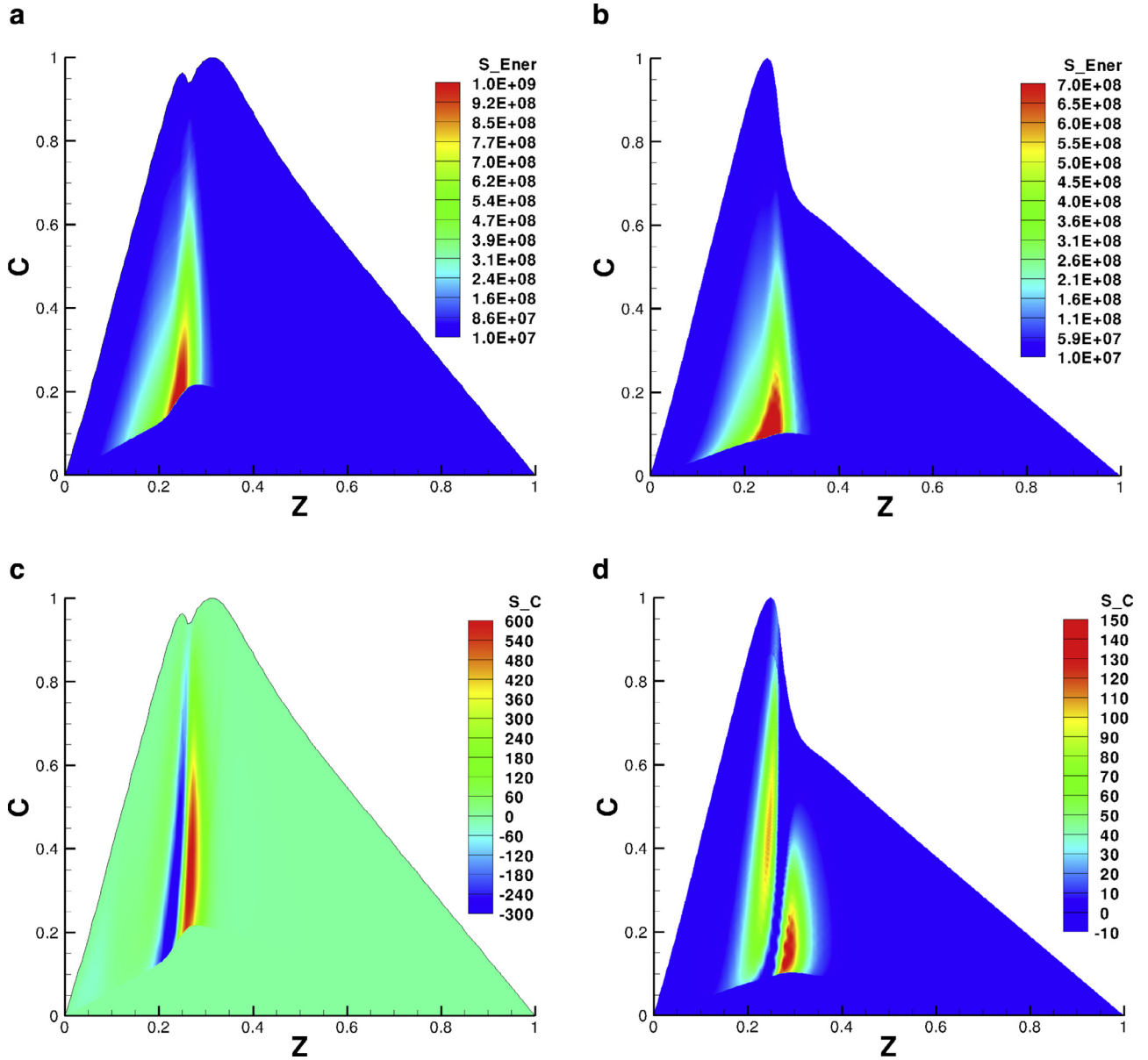


Fig. 9. Contour of the energy source term (W/m^3) in $C - Z$ space for (a) the steady FGM and (b) the unsteady FGM. As well as, the contour for the source term for C ($\text{kg/m}^3 - \text{s}$) for the (c) steady FGM and (d) the unsteady FGM.

where, \dot{S}_C''' is the source term for C that is pre-tabulated in the FGM. In addition, the energy equation is required for the compressible flow formulation and has an associated source/sink term, $\dot{S}_E''' = -\sum \dot{w}_i h_{f,i}^0$, which is also stored in the FGM. Figure 9(a) and (b) shows the source terms for energy for the steady and unsteady FGM, respectively. For both the steady and unsteady FGM, as the scalar dissipation rate is increased (decreasing Λ), the chemical source term increases due to flame dynamics shifting from a diffusion to a kinetically controlled burning. The major differences between the two are the relative magnitudes of the source terms, with the steady-state manifold containing source terms that are nearly a third larger than the unsteady manifold. The source term contours for the progress-variable can be seen in Fig. 9(c) and (d) for the steady and unsteady manifolds. The range of the progress-variable source term for the steady-state FGM is nearly 6-times that of the unsteady source term and the relative peak has shifted to a higher value of Z and is slightly angled for the unsteady case. The two peaks in the unsteady progress-variable source term seen

in Fig. 9(d) are due to a bimodal shape of \dot{S}_C''' as the diffusion flame progresses during the unsteady solution procedure.

Both *a priori* and *a posteriori* comparisons are conducted between the exact solutions and the steady FGM for $\dot{m}_T'' = 0$. The *a priori* tests are carried out using the finite-rate chemistry solution and reconstructing the progress-variables based on the definitions of Z and C used to populate the manifold. The values are then used to lookup species and source terms from the FGM and compared directly to the current solution. Results (not shown) from the *a priori* test indicate maximum errors of 0.5% and 0.8%, associated with interpolation errors. *A posteriori* comparisons involve transporting the mixture fraction and progress-variable and directly using \dot{S}_C''' and \dot{S}_E''' from the FGM in the solution. Comparisons of the finite-rate chemistry and the FGM solutions of temperature and major species are shown in Fig. 10(a) and minor species are shown in Fig. 10(b). As expected, good overall agreement is seen between the finite-rate chemistry solution and the FGM solution, with the maximum error of 2% occurring between the temperatures.

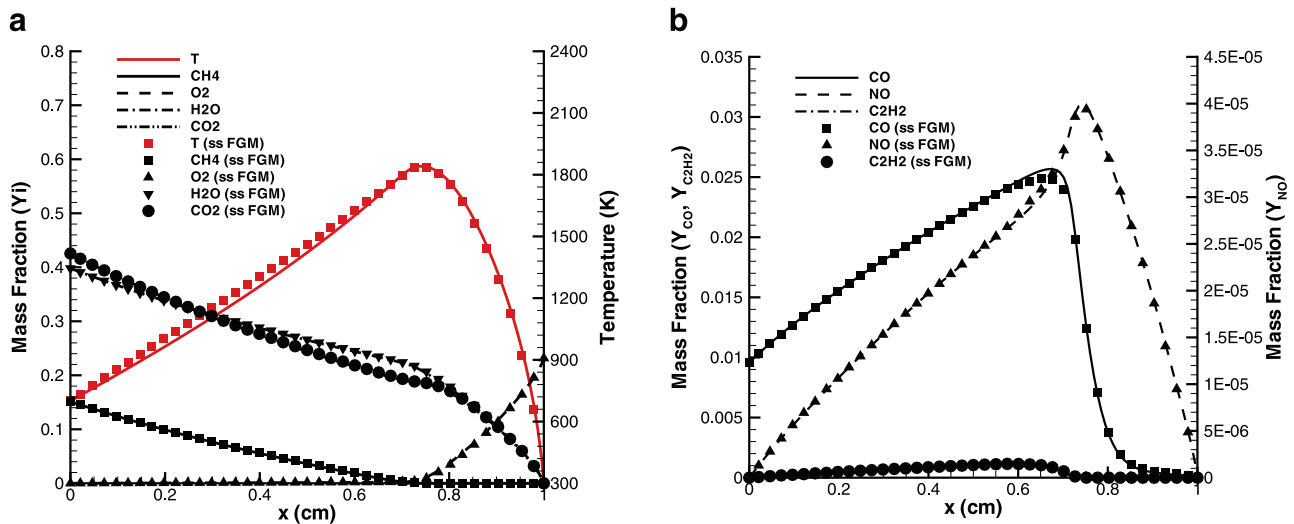


Fig. 10. *A posteriori* comparisons of (a) major species and temperature and (b) minor species of a 1D flame using the finite-rate chemistry (solid-lines) and the steady FGM (symbols).

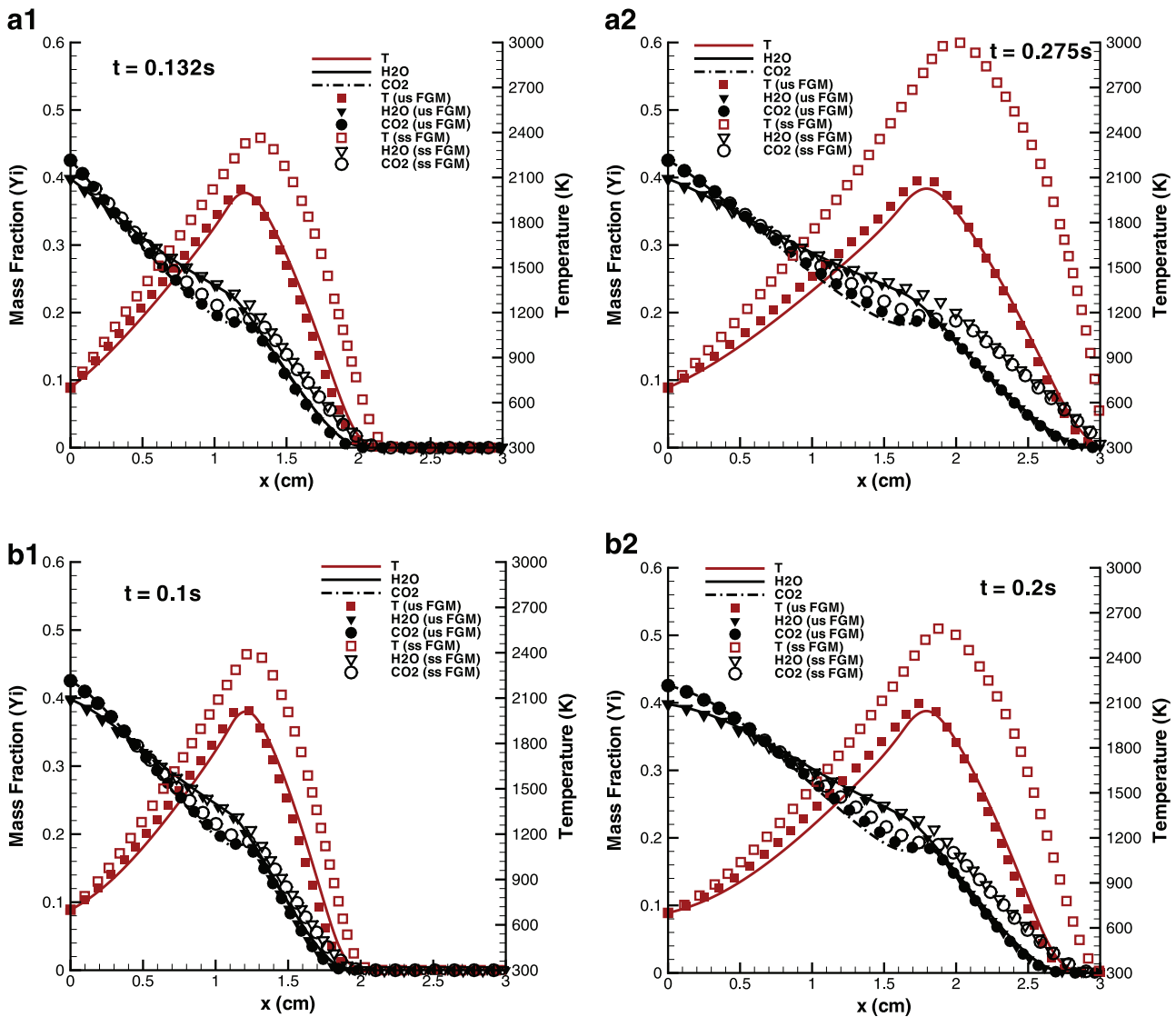


Fig. 11. Major species and temperature comparisons of the finite-rate chemistry (solid lines), the unsteady FGM (closed symbols) and the steady FGM (open symbols) at constant mass fluxes of (a) $0.01 \text{ (kg/m}^2 \cdot \text{s)}$ and (b) $0.02 \text{ (kg/m}^2 \cdot \text{s)}$ on a domain width of 3 cm.

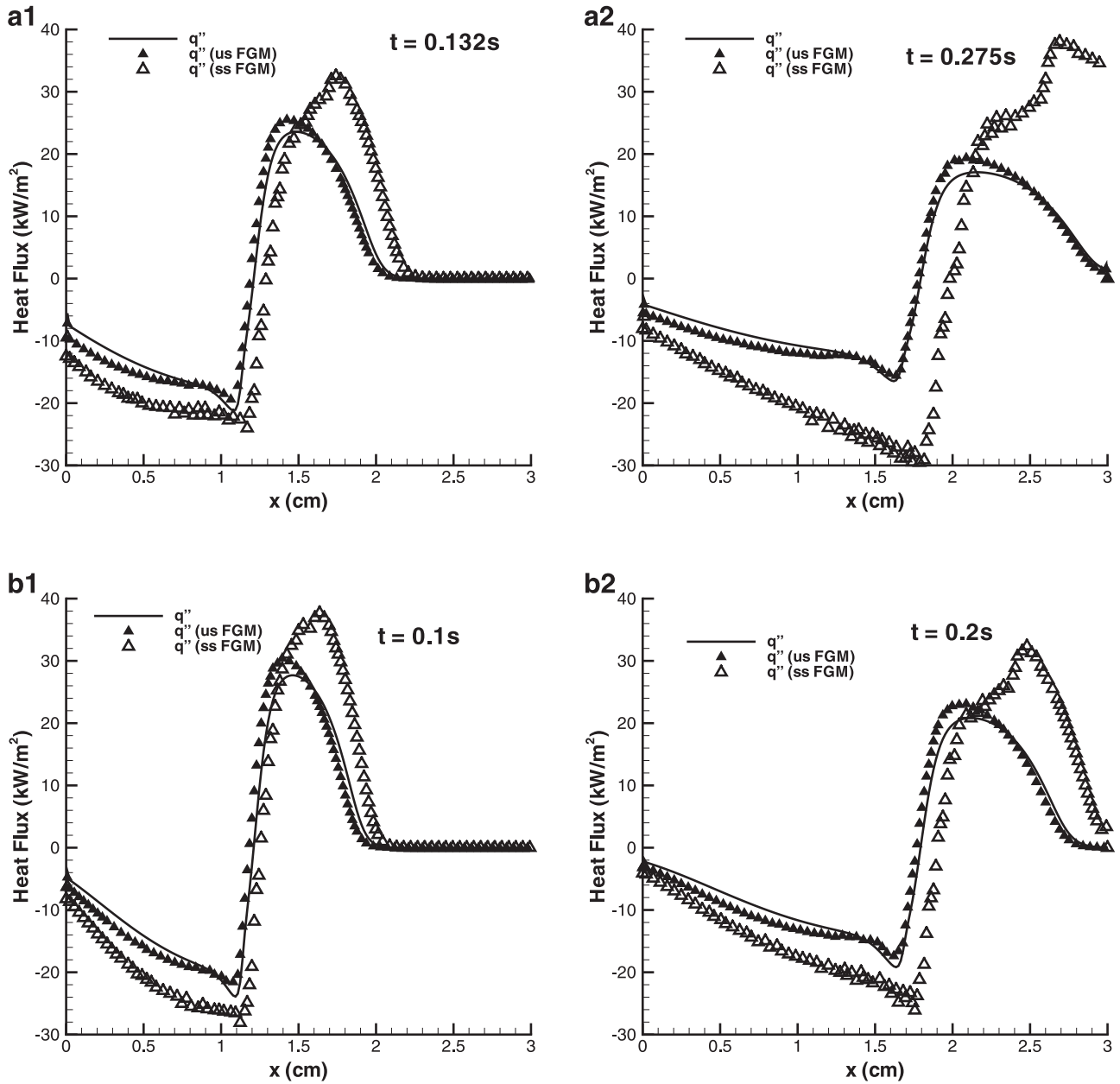


Fig. 12. Heat flux (kW/m^2) comparisons of the finite-rate chemistry (solid lines), the unsteady FGM (closed symbols) and the steady FGM (open symbols) at constant mass fluxes of (a) $0.01 \text{ (kg/m}^2 \cdot \text{s)}$ and (b) $0.02 \text{ (kg/m}^2 \cdot \text{s)}$ for a domain width of 3 cm.

Comparisons of the steady and unsteady FGM to the exact solution for each mass flux are shown in Fig. 11. Solutions are presented for when Z_{st} is located at 1.2 cm and 1.9 cm. Figure 11(a) shows the comparisons of H_2O , CO_2 , and T from the finite-rate chemistry (solid-lines), the unsteady FGM (closed symbols) and the steady FGM (open symbols) for the mass flux of $\dot{m}''_T = 0.01 \text{ kg/m}^2 \cdot \text{s}$. While the flame locations match up relatively well between the exact and steady FGM, the error in the major species and temperature are found to be 28% and 48%, respectively. Similar trends are observed in Fig. 11(b) for $\dot{m}''_T = 0.02 \text{ kg/m}^2 \cdot \text{s}$, where temperatures are over-predicted. The unsteady manifold represented with closed symbols in Fig. 11, greatly reduces associated errors with max errors in temperature, CO_2 and H_2O of 10%, 6%, and 7%, respectively.

It is interesting to note the insensitivity of the solution to the initial condition. Although the unsteady FGM was created considering the expansion of a flame starting from $\chi_{st} = 115 \text{ s}^{-1}$,

the reacting boundary solutions were started at an initial value of $\chi_{st} = 41 \text{ s}^{-1}$ and the results matched within a reasonable tolerance. The difference between the steady and unsteady solution then, is the relative trajectory of χ , where a steady FGM assumes that χ will evolve slowly [41]. By including the unsteady flame effects within the FGM, the unsteady trajectory of χ and the flame solution better match the exact solution to the reacting boundary.

Another critical component for accurately capturing the effects of reacting boundary layers with flamelet-generated manifolds, is the ability to capture the near-wall heat flux that will be used during the coupling procedure between the gas phase solution and the solid/liquid fuel boundary. The heat flux for the finite-rate chemistry (solid lines), the unsteady FGM (closed symbols) and the steady FGM (open symbols) solutions are shown in Fig. 12. The error in the heat flux between the steady manifold and the finite-rate chemistry can be as high as 130%, which could result in an error propagation of the resultant mass flux with coupling

in place. Applying the unsteady FGM results in an accurate match of the heat flux term when compared to the finite-rate chemistry solution, with the maximum error of 18%.

5. Conclusion

In this study, steady and unsteady FGM are developed for application to biomass combustion. The steady FGM are developed from a series of steady-state strained diffusion flames. Manifolds are generated based on the minimization of a cost function defined to achieve monotonicity and to expand the manifold in order to reduce source term gradients within the $\Lambda - Z$ space. Steady FGM comparisons are made with finite-rate chemistry solutions in *a posteriori* calculations and show overall good agreement, however it does not perform well for unsteady flames. A unique approach is introduced in this study to capture unsteady flame effects by tracking an expanding flame. The resulting unsteady FGM is then created with the same procedure used for the steady FGM and is compared to the exact solution. Applying the unsteady FGM proved to reduce errors in temperature and major species mass fractions significantly, resulting in errors that do not exceed 10% in both cases. The heat flux comparison is also within good approximation, with errors not exceeding 20%, when comparing the unsteady FGM and finite-rate chemistry and will be invaluable when applied to a more complicated reacting boundary flow problems.

Acknowledgments

Funding: Support for this work has been provided by the [New York State Energy Research and Development Authority \(NYSERDA\)](#) under contract number [#32966](#) and [NAVAIR](#) through the STTR phase II program under contract [N68335-10-C-0418](#)

References

- [1] J.A. Oijen, L.P.H. de Goeij, Modelling of premixed laminar flames using flamelet-generated manifolds, *Comb. Sci. and Technol.* 161 (2000) 113–137.
- [2] C.D. Pierce, Progress-variable approach for large-eddy simulation of turbulent combustion, Phd thesis, Stanford University, 2001.
- [3] C.D. Pierce, P. Moin, Progress-variable approach for large-eddy simulation of non-premixed turbulent combustion, *J. Fluid Mech.* 504 (2004) 73–97.
- [4] J.A. van Oijen, F.A. Lammers, L.P.H. de Goeij, Modeling of complex premixed burner systems by using flamelet-generated manifolds, *Combust. Flame* 127 (3) (2001) 2124–2134.
- [5] J.A. van Oijen, L.P.H. de Goeij, Modelling of premixed counterflow flames using the flamelet-generated manifold method, *Combust. Theory Model.* 6 (2002) 463–478.
- [6] L.M. Verhoeven, W.J.S. Ramaekers, J.A.V. Oijen, L.P.H. deGoeij, Modeling non-premixed laminar co-flow flames using flamelet-generated manifolds, *Combust. Flame* 159 (2012) 230–241.
- [7] E. Knudsen, H. Pitsch, A general flamelet transformation useful for distinguishing between premixed and non-premixed modes of combustion, *Combust. Flame* 156 (2009) 678–696.
- [8] H. Wu, Y.C. See, Q. Wang, M. Ihme, A pareto-efficient combustion framework with submodel assignment for predicting complex flame configurations, *Combust. Flame* 162 (2015) 4208–4230.
- [9] A.W. Vreman, B.A. Albrecht, J.A. van Oijen, L.P.H. de Goeij, R.J.M. Bastiaans, Premixed and nonpremixed generated manifolds in large-eddy simulation of sandia flame d and f, *Combust. Flame* 153 (3) (2008) 394–416.
- [10] M. Ihme, H. Pitsch, Prediction of extinction and reignition in nonpremixed turbulent flame using a flamelet/progress variable model 2. application in LES of sandia flames D and E, *Combust. Flame* 155 (2008) 90–107.
- [11] R.S. Barlow, J.H. Frank, A.N. Karpetsis, J.-Y. Chen, Piloted methane/air jet flames: Scalar structure and transport effects, *Combust. Flame* 143 (2005) 433–449.
- [12] C. Bekdemir, L.M.T. Somers, L.P.H. de Goeij, Modeling diesel engine combustion using pressure dependent flamelet generated manifolds, *Proc. Combust. Inst.* 33 (2011) 2887–2894.
- [13] J. Tillou, J.-B. Michel, C. Angelberger, D. Veynante, Assessing LES models based on tabulated chemistry for the simulation of diesel spray combustion, *Combust. Flame* 161 (2014) 525–540.
- [14] A. Wehrfritz, O. Kaario, V. Vuorinen, B. Somers, Large eddy simulation of n-dodecane spray flames using flamelet generated manifolds, *Combust. Flame* 167 (2016) 113–131.
- [15] M. Chrigu, J. Gounder, A. Sadiki, A.R. Masri, J. Janicka, Partially premixed reacting acetone spray using LES and FGM tabulated chemistry, *Combust. Flame* 159 (8) (2012) 2718–2741. Special Issue on Turbulent Combustion.
- [16] E. Knudsen, Shashank, H. Pitsch, Modeling partially premixed combustion behavior in multiphase LES, *Combust. Flame* 162 (1) (2015) 159–180.
- [17] W. Xie, P.E. Desjardin, A level set embedded interface method for conjugate heat transfer simulations of low speed 2d flows, *Comput. Fluids* 37 (2008) 1262–1275.
- [18] W. Xie, P.E. Desjardin, An embedded upward flame spread model using 2D direct numerical simulations, *Combust. Flame* 156 (2) (2009) 522–530.
- [19] C.K. Law, *Combustion physics*, Cambridge University Press, 2006.
- [20] M.-S. Liou, A sequel to AUSM, part ii: AUSM+UP for all speeds, *J. Comput. Phys.* 214 (1) (2006) 137–170.
- [21] Y. Li, Wavenumber-extended high-order upwind-biased finite-difference schemes for convective scalar transport, *J. Comput. Phys.* 133 (1997) 235–255.
- [22] J.A. Sethian, S.J. Osher, The design of algorithms for hypersurfaces moving with curvature-dependent speed, *Notes on numerical fluid mechanics*, 24 (1989).
- [23] G.P. Smith, D.M. Golden, M. Frenklach, N.W. Moriarty, B. Eiteneer, M. Goldenberg, C.T. Bowman, R.K. Hanson, S. Song, W.C. Gardiner Jr., V.V. Lissianski, Z. Qin, *Gri mech* 3.0.
- [24] W.C. Reynolds, Implementation in the interactive program STANJAN, Department of Mechanical Engineering, Stanford University (January 1986).
- [25] M. Bajus, Pyrolysis of woody material, *Petrol. Coal* 52 (3) (2010) 207–214.
- [26] E. Grieco, G. Baldi, Analysis and modelling of wood pyrolysis, *Chem. Eng. Sci.* 66 (2011) 650–660.
- [27] T. Pattanotai, H. Watanabe, K. Okazaki, Experimental investigation of intraparticle secondary reactions of tar during wood pyrolysis, *Fuel* 104 (2013) 468–475.
- [28] L. Wei, S. Xu, L. Zhang, H. Zhang, C. Liu, H. Zhu, S. Liu, Characteristics of fast pyrolysis of biomass in a free fall reactor, *Fuel Process. Technol.* 87 (2006) 863–871.
- [29] J.-B. Michel, O. Colin, D. Veynante, Modeling ignition and chemical structure of partially premixed turbulent flames using tabulated chemistry, *Combust. Flame* 152 (1–2) (2008) 80–99.
- [30] M. Ihme, L. Shuun, J. Zhang, Regularization of reaction progress variable for application to flamelet-based combustion models, *J. Comput. Phys.* 231 (2012) 7715–7721.
- [31] W.H. Press, S.A. Teukolsky, W.T. Vetterling, B.P. Flannery, *Numerical recipes: the art of scientific computing*, Cambridge University Press, 2007.
- [32] S. Delhay, L.M.T. Somers, J.A. van Oijen, L.P.H. de Goeij, Incorporating unsteady flow-effects in flamelet-generated manifolds, *Combust. Flame* 155 (2008) 133–144.
- [33] S. Delhay, L.M.T. Somers, J.A. van Oijen, L.P.H. de Goeij, Incorporating unsteady flow-effects beyond the extinction limit in flamelet-generated manifolds, *Combust. Flame* 32 (2009) 1051–1058.
- [34] P.-D. Nguyen, L. Vervisch, V. Subramanian, P. Domingo, Multidimensional flamelet-generated manifolds for partially premixed combustion, *Combust. Flame* 157 (2010) 43–61.
- [35] H. Pitsch, M. Chen, N. Peters, Unsteady flamelet modeling of turbulent hydrogen-air diffusion flames, *Symp. (Int.) Combust.* 27 (1998) 1057–1064.
- [36] G. Lodier, L. Vervisch, P. Moureau, P. Domingo, Composition-space premixed flamelet solution with differential diffusion for in situ flamelet-generated manifolds, *Combust. Flame* 158 (2011) 2009–2016.
- [37] T. Kim, Y. Kim, Interactive transient flamelet modeling for soot formation and oxidation processes in laminar premixed jet flames, *Combust. Flame* 162 (2015) 1660–1678.
- [38] M. Ihme, Y.C. See, Prediction of autoignition in a lifted methane/air flame using an unsteady flamelet/progress variable model, *Combust. Flame* 157 (2010) 1850–1862.
- [39] Y. Yener, S. Kakac, *Heat conduction*, fourth edition, Taylor and Francis, 2008.
- [40] D. Drysdale, *An introduction to fire dynamics*, John Wiley and Sons, New York, NY, 1998.
- [41] N. Peters, *Turbulent combustion*, Cambridge University Press, Cambridge, UK, 2000.